Combustion and Flame 294 (2026) 115339

Contents lists available at ScienceDirect

Combustion and Flame

journal homepage: www.sciencedirect.com/journal/combustion-and-flame

Detonation instability mechanisms under transverse dilution jets in rotating detonation turbine engines

Yuechen Hou [a], Qi Sun [a], Yingnan Wang [b], Yiting Dang [a], Zhuang Ma [a], Zheng Chen [a], Jianping Wang [a,*]

[a] Center for Combustion and Propulsion, SKLTCS, CAPT, HEDPS, School of Mechanics and Engineering Science, Peking University, Beijing 100871, China
[b] College of Engineering, Peking University, Beijing 100871, China

ARTICLE INFO

Keywords:
Rotating detonation turbine engine
Transverse dilution jet
Wave collision mode
Detonation instability

ABSTRACT

Effective air dilution for turbine inlet cooling without compromising detonation stability is essential yet challenging for rotating detonation turbine engines (RDTEs). This study investigates detonation instability mechanisms under downstream transverse dilution jets in a methane-fueled open-loop RDTE. Air jets introduced during operation raise combustor pressure and suppress reactant accumulation, leading to transient wave attenuation or detonation decoupling under stronger dilution. Under kilohertz oblique-shock sweeping, transverse jets undergo periodic blockage and penetration, producing non-uniform cold-air packets that break the wave-strength balance in four-wave collision modes. RDTE experiments show that jet-wave coupling is governed by the jet recovery timescale relative to successive detonation sweeping, rather than by air flow rate alone. When the two timescales become comparable, the jets recover and penetrate more deeply, promoting detonation mode adjustment. The resulting feedback between energy loss caused by dilution disturbance and energy gain associated with reactant accumulation periodically adjusts wave strength, driving wave-spacing oscillation between co-propagating detonation waves. This intermediate regime between stable propagation and complete instability provides a new perspective on mode stability boundaries in RDTEs under air dilution disturbances.

Novelty and significance statement

Effective air dilution is essential for turbine inlet cooling in rotating detonation turbine engines (RDTEs). Existing studies mainly address cooling feasibility, leaving its influence on detonation stability unresolved. This study develops a methane-fueled RDTE with secondary-air injection, extends RDTE research beyond the hydrogen fuel, and achieves sustained engine operation over 2 min. The detonation instability mechanisms induced by transverse air jets under sustained turbine-coupled operation are revealed for the first time. Unlike quasi-steady mixing in conventional combustors, dilution jets are found to act as unsteady aerodynamic disturbances coupled to kilohertz detonation-wave propagation. A key novelty is identifying the relative timescale of jet recovery and detonation sweeping as the governing parameter for instability onset, and elucidating the self-sustained mechanism of wave-spacing oscillations. These findings provide a physical basis for balancing turbine cooling requirements against detonation stability constraints in RDTEs.

1. Introduction

Rotating detonation combustors (RDCs) have emerged as a promising pressure-gain combustion technology [1,2] for advanced propulsion systems, sustaining one or more detonation waves (DWs) traveling azimuthally at kilohertz frequencies under continuous reactant injection [1,3]. Integration of RDCs with compressor and turbine components enables rotating detonation turbine engines (RDTEs) with potentially higher thermal efficiency [2,4], lower specific fuel consumption [5], fewer compressor stages, and more compact combustors [6], but remains technically challenging.

Most RDTE integration studies have adopted open-loop configurations supplied by external air rather than an actual compressor [7–12]. This approach avoids the intense upstream pressure feedback from DWs and the associated risk of compressor surge in closed-loop operation. Hydrogen/air mixtures have also been primarily used for ease of

* Corresponding author.
E-mail address: wangjp@pku.edu.cn (J. Wang).

https://doi.org/10.1016/j.combustflame.2026.115339
Received 4 June 2026; Received in revised form 22 September 2026; Accepted 22 September 2026
Available online 10 October 2026
0010-2180/© 2026 The Combustion Institute. Published by Elsevier Inc. All rights are reserved, including those for text and data mining, AI training, and similar technologies.

detonation, despite hydrogen being less attractive than hydrocarbon fuels in storage and cost [13]. Early RDTE demonstrations were primarily based on turboshaft engines to minimize RDC modifications [7–9, 14,15]. Recent studies further extended RDTE integration to disk combustors [16,17] and turbojet engines with annular combustors [10,11], yet most efforts employed simplified engine configurations and focused primarily on detonation propagation characteristics.

Turbine inlet cooling remains another critical challenge to RDTE integration. To maintain stable rotating detonation, near-stoichiometric mixtures are usually required. This results in an exhaust temperature much higher than that of conventional constant-pressure combustors [12,18,19]. Downstream air dilution is therefore essential for turbine inlet temperature control in highly unsteady detonation exhaust with oblique shocks. Frolov et al. [19] numerically showed that radially injected secondary air markedly reduces temperature fluctuations at the RDC outlet. Naples et al. [14] employed an ejector to entrain cooling air utilizing the exhaust momentum, reducing exhaust pressure oscillations by 60%–70%. Wang et al. [12] reported that jet cooling lowered the turbine inlet temperature from about 2076 K to 1561 K but remained inadequate for sustained turbine operation.

However, these studies have largely focused on the feasibility of exhaust cooling. Only limited studies have examined the effects of downstream dilution air on RDC performance. Bykovskii et al. [6] showed that air supplied normal to the product flow increases combustor pressure and thrust, and also increases the number of DWs and introduces additional total pressure losses through shock interactions and heat exchange. He et al. [20] experimentally reported that larger dilution hole areas increase the RDC total pressure gain. Nevertheless, existing studies remain confined to combustors rather than turbine-coupled operation, and the influence of downstream dilution on detonation stability has received little attention.

Unlike film cooling, which favors wall-attached coolant coverage [21,22], dilution requires sufficient jet penetration and mixing to condition the turbine inlet flow [23]. The interaction mechanism between transverse dilution jets and rotating detonation waves differs fundamentally from the classical jet-in-crossflow problem [24,25] or quasi-steady jet mixing in conventional combustors. In a RDC, oblique shocks and detonation products sweep across dilution holes at kilohertz frequencies, periodically causing jet blockage, penetration, recovery, and possible product backflow. Thus, DW propagation governs the transient jet response, while the dilution jets in turn affect detonation stability.

The objective of this study is to reveal the instability mechanisms of rotating detonation under downstream transverse dilution jets, and establish a physical basis for balancing turbine inlet cooling against detonation stability limits. We develop an open-loop methane-fueled RDTE, with detonation exhaust driving the turbine. Methane is selected as an intermediate fuel [26–28] toward future kerosene-fueled operation [29], while avoiding the additional atomization and evaporation complexities of liquid fuels. Detonation attenuation and subsequent recovery under runtime dilution are first characterized (Section 3). Four-wave collision dynamics and rotor response are then examined. Transient mode analysis further shows that dilution jets break the wave-strength balance in four-wave collision modes and induce wave-spacing oscillations (Section 4). Finally, the onset of wave-spacing oscillations is interpreted via the competition between jet recovery and detonation sweeping, whereas their persistence is explained by dynamic feedback among reactant injection, dilution jet penetration, and detonation strength adjustment (Section 5).

2. Experimental methodology

2.1. Integrated RDTE with secondary air

The integrated RDTE, shown in Fig. 1(a), is developed based on a 600 N-class turbojet engine, comprising an intake duct, centrifugal compressor, diffuser, single-stage turbine, and annular RDC with primary and dilution zones. DWs are sustained in the primary zone supplied with methane and oxygen-enriched air. Oxygen-enriched air compensates for the low reactivity of methane/air, whose large detonation cell size [30] prevents DW formation in the present annular RDC. An oxygen mole fraction X_{O_2} of 30% represents modest enrichment above that of air [26,27]. To ensure stable reactant delivery, an open-loop configuration is adopted, in which methane and oxygen-enriched air are supplied from separate high-pressure cylinders to the respective upstream plenums, thereby decoupling reactant delivery from the compressor.

The turbine is driven by detonation products and rotates the compressor through a common shaft. The blue arrows in Fig. 1(a) indicate the compressor air flow: the ambient air is compressed, passes through the semi-enclosed casing, then is discharged through a throttle valve. A fraction of the compressed air is routed through the shaft tube for bearing cooling. The turbine rotor consists of 31 subsonic blades. The rotor speed is measured in real time by a Hall-effect sensor mounted on the compressor shaft, which outputs voltage pulses proportional to rotational frequency. The maximum rotor speed is limited by the low inlet mass flow relative to practical aero-engines, and is further restricted for safety by partially closing the compressor throttle valve to increase the shaft load.

2.2. Rotating detonation combustor

The combustor and stator regions highlighted in Fig. 1(a) are detailed in Fig. 1(b). The annular combustor has a channel height of 236.5 mm, an outer radius R_o of 90 mm, and an annulus width of 35 mm. The turbine radius is 67 mm, leaving a 23 mm annular gap for aft-view optical access. The primary zone is defined from the injection plane to the first secondary-air hole row, yielding a length of 112.7 mm. Methane is injected through 90 holes of 0.8 mm diameter and the oxygen-enriched air via a circumferential slot with a width of 0.6 mm, forming a non-premixed crossflow injection configuration [31,32]. The mass flow rates of methane and oxygen-enriched air, $\dot{m}_f$ and $\dot{m}_a$, are measured by Coriolis flow meters with measurement ranges of 0–213 g/s and 0–800 g/s and an accuracy of ±0.25% FS. The global equivalence ratio in the primary zone is defined as $\varphi_p = 2\,(\dot{m}_f/M_f)/(\dot{m}_a/M_a\,X_{O_2})$, where M_f and M_a denote the molar masses. The total mass flow rate is $\dot{m}_{tot} = \dot{m}_a + \dot{m}_f$.

Secondary air is supplied independently from gas cylinders to an annular air plenum and injected into the dilution zone through film-cooling (2 mm-diameter) and dilution holes, without affecting primary-zone reactant delivery. Three axial rows of twelve dilution holes, each with a diameter of $d_{hole} = 10$ mm, are located 172.7, 192.7, and 212.7 mm downstream of the injection plane to minimize their influence on detonation propagation [6,21]. The air volumetric flow rate ($\dot{V}_{air}$) is measured via a spiral vortex flowmeter (±1.5% reading accuracy) and controlled by the opening of a pressure-reducing valve (η_{air}). $\dot{V}_{air}$ can be converted to a mass flow rate as $\dot{m}_{air} = \dot{V}_{air} M_{air}/V_0$, where V_0 is the standard molar volume and M_{air} is the molar mass of air. Valve openings of η_{air} = 15%–40% give $\dot{m}_{air}$ = 95–250 g/s.

Two combustors are used for the short- and long-duration RDTE tests. The short-duration tests employ the brass combustor shown in Fig. 1(b), instrumented with multiple sensors to examine the effects of dilution air on detonation stability. The circumferential arrangement of the pressure ports located 47.5 mm downstream of the injection plane is shown in Fig. 1(c). Two flush-mounted piezoelectric pressure sensors (PCB1 and PCB2), positioned 90° apart on the outer wall, sample the combustor dynamic pressure at 1 MHz. A pressure transmitter installed in a capillary tube average pressure (CTAP) configuration, with a measurement range of 0–20 bar and an accuracy of 0.2% FS, measures the combustor absolute pressure p_c at 4 kHz. Three additional CTAP transmitters monitor the pressure in the fuel plenum, oxidizer plenum, and secondary-air plenum (p_{air} in Fig. 1(b)), respectively. A Phantom V611 high-speed camera (HSC) positioned 5 m downstream of

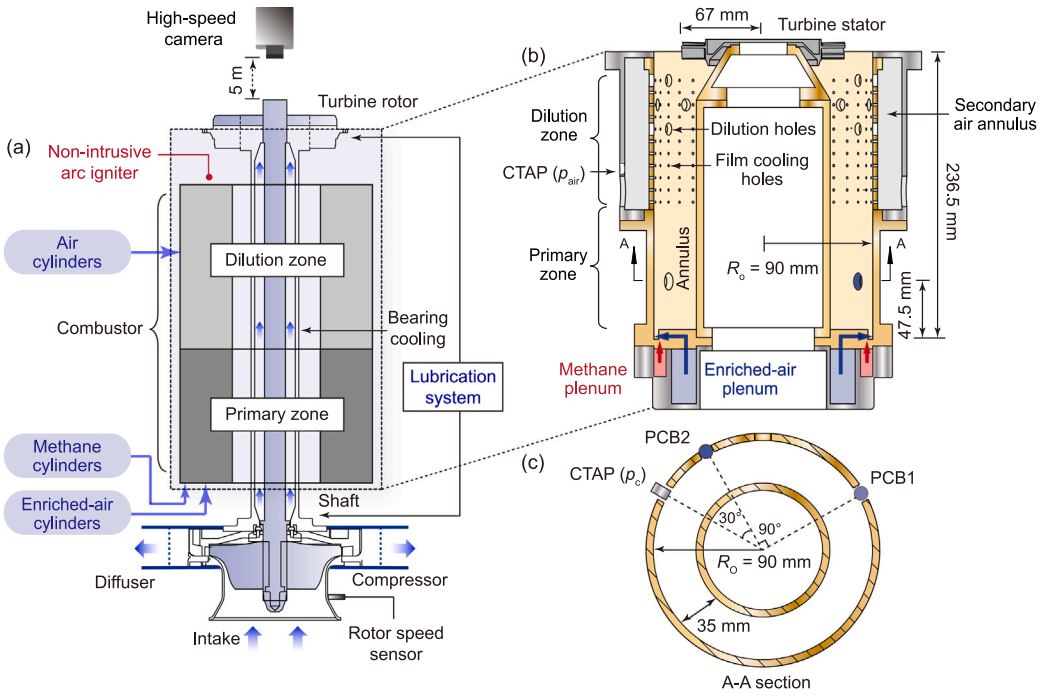


Fig. 1. Schematic of (a) the open-loop integrated RDTE and (b) combustor-stator assembly highlighted by the dashed box in (a); (c) the circumferential arrangement of pressure measurement ports.

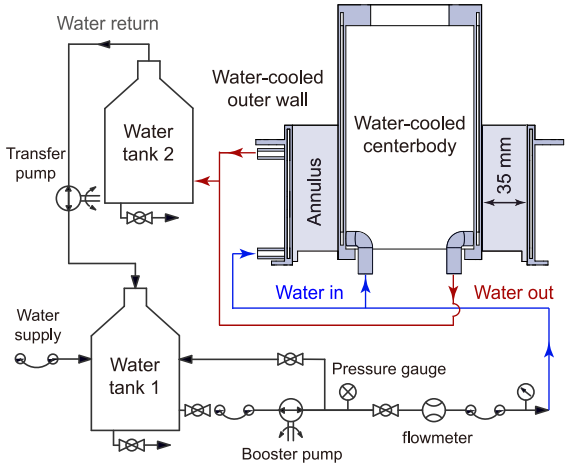


Fig. 2. Schematic of the water-cooled RDTE combustor and coolant circulation system.

the RDTE records DW self-luminescence at 50000 fps with a 256 × 256 pixel resolution. A video camera placed beside the RDTE records engine operation and the exhaust plume, with audio sampled at 48 kHz.

For long-duration RDTE operation, the combustor is replaced by actively-cooled outer wall and centerbody with internal water passages (Fig. 2). The outer wall combines water cooling in the high heat-flux detonation region with downstream film cooling, whereas the centerbody is fully water cooled. The circulation system sustains a water flow rate of 1.4 kg/s. Pressurized water from Tank 1 is divided to the inner and outer wall channels. The heated water is then collected in Tank 2, cooled, and returned to Tank 1 for reuse. To support thin-wall combustor and uniform wall-cooling design, the RDTE employs a retractable arc igniter with a 15 kV discharge at the combustor exit (Fig. 1(a)) for non-intrusive ignition [27,28].

Table 1 summarizes four short-duration tests with X_{O_2} = 30% and $\varphi_p \approx 1$, while $\dot{m}_{tot}$ remains nearly constant with relative standard deviations below 3%. The dilution effects can therefore be assessed mainly by varying $\dot{m}_{air}$. The sensors and HSC are triggered simultaneously at $t = 0$, and the arc igniter operates from $t = 0$ to 0.5 s, after which the RDTE continues to operate for 2.5 s. Two secondary-air injection strategies are compared. For pre-ignition dilution, secondary air is introduced at $t = -7$ s and maintained throughout the test. For runtime dilution, air injection begins at $t \approx 1.5$ s, after self-sustained DWs are established. Case E5 further demonstrates long-duration RDTE operation of 127 s at $\varphi_p = 0.70$. X_{O_2} is increased to 35% to sustain detonation under the leaner condition and pre-ignition dilution.

3. Detonation attenuation and recovery under air injection

Fig. 3(a) illustrates the typical combustor pressure response to runtime dilution in Case E3, where transverse air jets transiently perturb established DWs. The high-frequency PCB2 signal, corrected for thermal drift and low-pass filtered at 20 kHz, is plotted as relative dynamic pressure with a redefined zero level [33,34]. After air injection at $t \approx 1.5$ s, the pressure peaks drop abruptly, indicating transient detonation attenuation. As shown in Fig. 3(b), a partial recovery follows a detonation interruption interval t_{int}, defined by the absence of the dominant frequency in the short-time Fourier transform (STFT) spectrum (10 ms sliding window, 95% overlap). Nevertheless, the recovered peak pressure p_d remains lower than the value p_o before dilution. The effects of dilution on detonation strength are quantified in Fig. 3(c) using t_{int} and the ratio of time-averaged peak pressures after and before dilution, $\bar{p}_d/\bar{p}_o$. As $\dot{m}_{air}$ increases from Case E2 to E4, $\bar{p}_d/\bar{p}_o$ decreases, indicating progressively stronger detonation attenuation. Meanwhile, t_{int} increases from 0 to 0.38 s, showing a longer delay in detonation re-establishment as the air flow rate increases.

The detonation attenuation and subsequent recovery result from the coupled response of combustor pressure and reactant injection. As dilution starts, the air-plenum pressure p_{air} rises sharply (Fig. 3(d)). The transverse jets restrict the effective exhaust area, increasing the combustor pressure p_c (Fig. 3(e)). With increasing $\dot{m}_{air}$ in Cases E2–E4

Table 1
Experimental conditions.

Case	X_{O_2}	$\dot{m}_{tot}$ (g/s)	φ_p	Dilution timing	η_{air}	$\dot{m}_{air}$ (g/s)	Duration
E1	30%	193	0.95	Pre-ignition	15%	95	2.5 s
E2	30%	204	1.00	Runtime	20%	130	2.5 s
E3	30%	202	0.98	Runtime	30%	202	2.5 s
E4	30%	192	1.00	Runtime	40%	250	2.5 s
E5	35%	172	0.70	Pre-ignition	15%	90	127 s

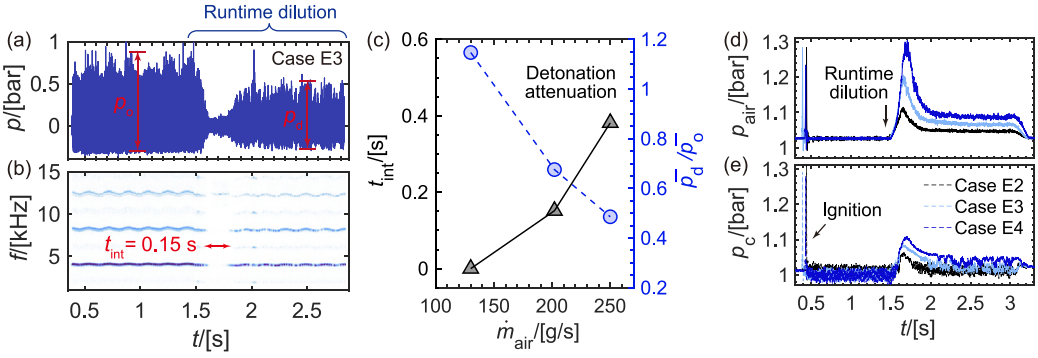


Fig. 3. (a) PCB2 signal and (b) STFT spectrum for Case E3; (c) ratio of time-averaged peak pressure $\bar{p}_d/\bar{p}_o$ and detonation interruption interval t_{int} versus $\dot{m}_{air}$; evolutions of (d) air plenum pressure p_{air} and (e) combustor pressure p_c in Cases E2–E4.

(η_{air} = 20%, 30%, and 40%), p_{air} peaks at 1.1, 1.2, and 1.3 bar, while p_c rises to 1.06, 1.08, and 1.10 bar, respectively. The elevated p_c reduces the reactant injection pressure drop and the accumulation height ahead of the DWs. Detonation is therefore attenuated. Under stronger dilution, the reactant height falls below the threshold for self-sustained detonation propagation, causing transient decoupling and thrust interruption, as observed in Cases E3 and E4. As the weakened DWs reduce p_c, the injection pressure drop is partially restored, promoting reactant refilling, shock-flame re-coupling, and gradual detonation strength recovery. p_{air} and p_c also stabilize at 1.05–1.09 bar and 1.01–1.04 bar. These indicate that determining the secondary-air mass flow rate requires balancing turbine cooling against detonation sustainability.

4. Detonation mode evolution under air injection

4.1. Four-wave collision dynamics and rotor response

The detonation instability induced by secondary-air injection evolves from the baseline mode before dilution, namely, the four-wave collision mode with collision-point migration (4CR-CPM) in Cases E1–E4. Case E2 is first examined to elucidate the four-wave collision dynamics and the associated rotor response. The HSC frame in Fig. 4(a), acquired at t = 2.90122 s, captures synchronous collisions between the clockwise (CW) and counter-clockwise (CCW) wave pairs at A1 and A2. The pressure rise associated with wave collision temporarily suppresses reactant injection, causing local wave decoupling. As the injection recovers, the detonation fronts are re-established. After propagating circumferentially by 90°, the waves collide again at A1'/A2', as recorded in Fig. 4(b). The counter-clockwise rotating turbine blades are captured simultaneously in Figs. 4(a)(b) after being heated by the high-temperature detonation products.

The space–time ($x - t$) diagrams in Figs. 4(c)(d) are constructed from HSC frames by radially averaging luminosity between the white dotted annular boundaries in Figs. 4(a)(b). The axes denote time and angular coordinate α. Based on the sampling region including the blade tips in Fig. 4(a), Fig. 4(c) shows superposed DW and rotor trajectories. The low-slope luminous traces correspond to the 31 turbine blades (N_v = 31). To isolate the DW trajectories without the blade signatures, the sampling region in Fig. 4(b) excludes the blade tips. Fig. 4(d) therefore shows only the DW paths marked by blue (CW pair) and yellow (CCW pair) lines. The drifting intersections of criss-cross DW trajectories indicate clockwise collision-point migration in 4CR-CPM mode driven by wave-strength imbalance. All subsequent $x-t$ diagrams use the combustor sampling region in Fig. 4(b).

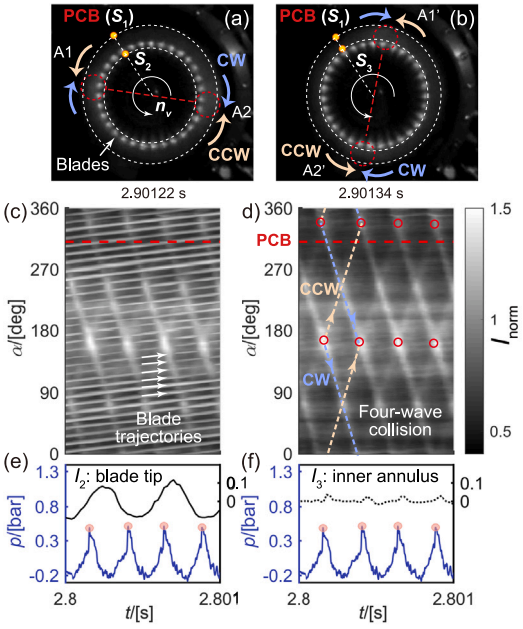


Fig. 4. (a)(b) Successive HSC frames of four-wave collision; space–time diagrams depicting (c) both detonation propagation and turbine blade trajectories, and (d) the isolated DW propagation paths; (e)(f) normalized luminous intensity sampled at blade tip (I_2) and the inner annulus (I_3) and the synchronous PCB2 signal in Case E2.

The normalized luminous intensity ($I_{norm} = (I - I_{min})/(I_{max} - I_{min})$) is extracted from HSC frames. At the blade-tip location S_2 (Fig. 4(a)), the peaks in I_2 coincide with successive blade passages (Fig. 4(e)). In contrast, as shown in Fig. 4(f), I_3 sampled at S_3 within the combustor annulus (Fig. 4(b)) exhibits weaker fluctuations without pronounced blade-passage peaks, coincide with the pressure spikes produced by

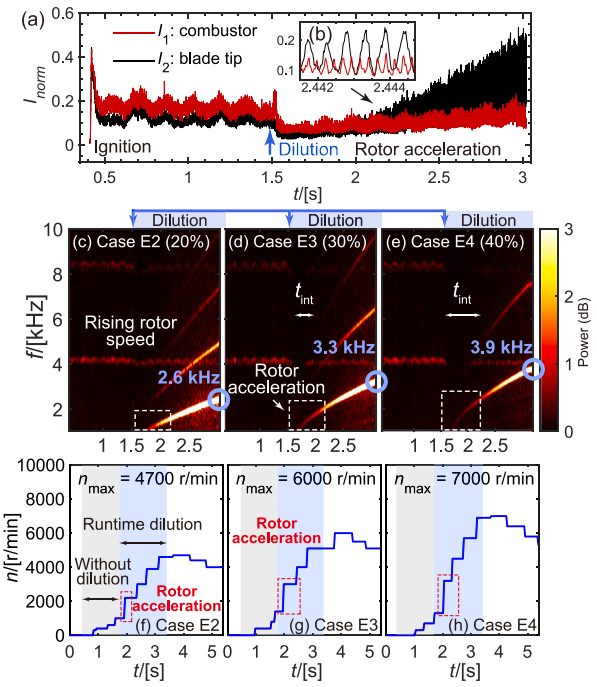


Fig. 5. (a) I_{norm} evolution at the combustor outer wall (I_1) and blade tip (I_2), enlarged in (b), for Case E2. (c)(d)(e) STFT spectra of the normalized luminous intensity I_{norm} at the blade tip (I_2) in Cases E2, E3, and E4. (f)(g)(h) Corresponding rotor-speed histories measured by the Hall sensor.

collision-point passages near PCB2 ($\alpha = 310°$). Fig. 5(a) further shows the luminous intensity histories sampled at the combustor outer wall (I_1) and blade tip (I_2) throughout the Case E2 test. I_1 exceeds I_2 before $t = 1.5$ s; air injection then attenuates both signals. Continuous exposure to high-temperature detonation products heats the turbine blades and intensifies their thermal radiation, causing I_2 to progressively exceed I_1, as detailed in Fig. 5(b).

The STFT spectra of I_2 for Cases E2, E3, and E4 in Figs. 5(c)(d)(e) identify dominant blade-passing frequencies (f_v), defined as the frequency at which successive blade tips pass the sampling location S_2. The rotor speed can be estimated as

$$n_v = 60\frac{f_v}{N_v}. \tag{1}$$

At higher $\dot{m}_{air}$, Cases E3 and E4 subsequently exhibit transient detonation quenching intervals (t_{int}). During RDTE operation, f_v reaches 2.6, 3.3, and 3.9 kHz, corresponding to $n_v \approx 5030$, 6390, and 7550 rpm in Cases E2, E3, and E4. These increases do not shift the detonation propagation frequency. Since the rotor revolution period ($T_{rev} = 60/n_{max} \approx 8$–12 ms) spans about 17–24 detonation propagation periods ($T_D = 0.49$–0.494 ms), the detonation modes remain largely insensitive to rotor motion, and the blades therefore act as a quasi-steady outlet restriction for the RDC. Moreover, dilution air injection at $t \approx 1.5$ s produces a rapid increase in f_v, indicating transient rotor acceleration (white boxes in Figs. 5(c)(d)(e)) under the combined momentum flux of the detonation products and dilution air.

For comparison, the rotor-speed histories measured by the Hall sensor are shown in Figs. 5(f)(g)(h), with the undiluted and diluted stages shaded gray and blue. As $\dot{m}_{air}$ increases, the maximum rotor speed rises to 4700 rpm, 6000 rpm, and 7000 rpm in Cases E2, E3, and E4, respectively. These values are slightly lower than those derived from the HSC frames. The difference may result from the 100 rpm resolution of the Hall sensor readouts, which may not resolve the instantaneous peak speed. The transient rotor acceleration upon dilution, highlighted by the red boxes, agrees with the STFT results in Figs. 5(c)(d)(e).

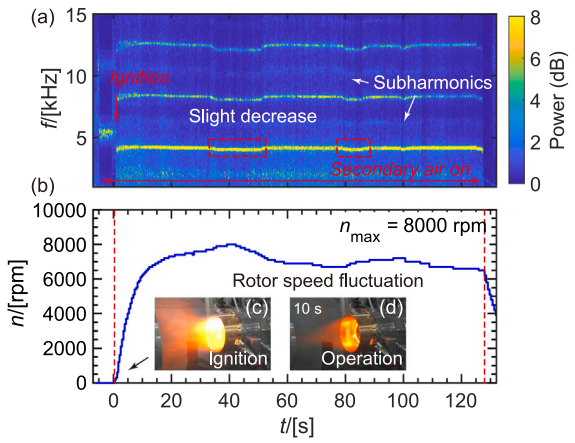


Fig. 6. Long-duration operation of the RDTE: (a) STFT spectrum of the acoustic signal; (b) synchronized temporal evolution of rotor speed; exhaust plumes during (c) ignition and (d) stable operation.

To allow the rotor to approach quasi-steady operation, the RDTE was operated for 127 s in Case E5, with the actively water-cooled combustor shown in Fig. 2 and pre-ignition dilution. The STFT spectrum of the acoustic signals extracted from the video recording in Fig. 6(a) indicates that the dominant frequency remains approximately stable at $f_p = 4.18$ kHz. This corresponds to a wave velocity of approximately 1181.9 m/s, or 58% of the theoretical Chapman-Jouguet (CJ) velocity V_{CJ} (calculated via Gaseq [35] at 1 bar and 300 K) in a four-wave collision mode. Slight decreases in f_p during $t = 34$–53 s and 77–87 s result from the oscillations in methane mass flow rates. After ignition, the rotor accelerates to 6600 rpm within 12 s and reaches a maximum speed of $n_{max} = 8000$ rpm at $t \approx 40$ s (Fig. 6(b)). The turbine then maintains a relatively stable output. The exhaust plume in Figs. 6(c)(d) provides further evidence of sustained detonation propagation.

4.2. Transient detonation mode adjustment

Instability in wave-collision modes arises from strength imbalances of the colliding DWs, typically manifested as collision-point migration (CPM). Fig. 7 first relates CPM dynamics to periodic peak bifurcation in the high-frequency pressure signals for the subsequent transient mode analysis. The $x - t$ diagram in Fig. 7(a) indicates collision points migrating counter-clockwise at a nearly constant velocity in Case E2 before runtime dilution. For synchronous PCB1 and PCB2 signals in Figs. 7(b)(c), CPM produces characteristic "X-shaped" variations (Figs. 7(d)(e)) in the time intervals between successive pressure peaks, $\delta t_{peaks,n} = t_{peak,n+1} - t_{peak,n}$, where n indexes the detected peaks. The "X-shaped" pattern arises because adjacent peak intervals vary oppositely as the collision point moves relative to the sensor, while satisfying

$$\delta t_{peaks,n} + \delta t_{peaks,n+1} \approx T_D/2, \tag{2}$$

where T_D is the detonation propagation period. At a maximum relative angular deviation of 45° from the sensor ($t = 0.839$–0.840 s), the equal intervals $\delta t_{peaks,n} = \delta t_{peaks,n+1} = T_D/4$ define the crossing intersection of the "X-shaped" pattern.

After 90° migration, the next collision point aligns with the sensor and δt_{peaks} returns to $T_D/2$. Thus, each "X-shaped" pattern can be approximately associated with a 90° azimuthal shift of collision-points relative to the sensor, yielding a CPM period of $T_{CPM} \approx 5$ ms. δt_{peaks} therefore serves as an effective indicator for tracking CPM in wave-collision regimes [28,36]. The nearly identical "X-shaped" patterns in Figs. 7(d)(e) for PCB1 and PCB2 further reflect the 90° azimuthal symmetry of the four-wave collision mode. PCB2 pressure signal is taken as representative in the subsequent analysis.

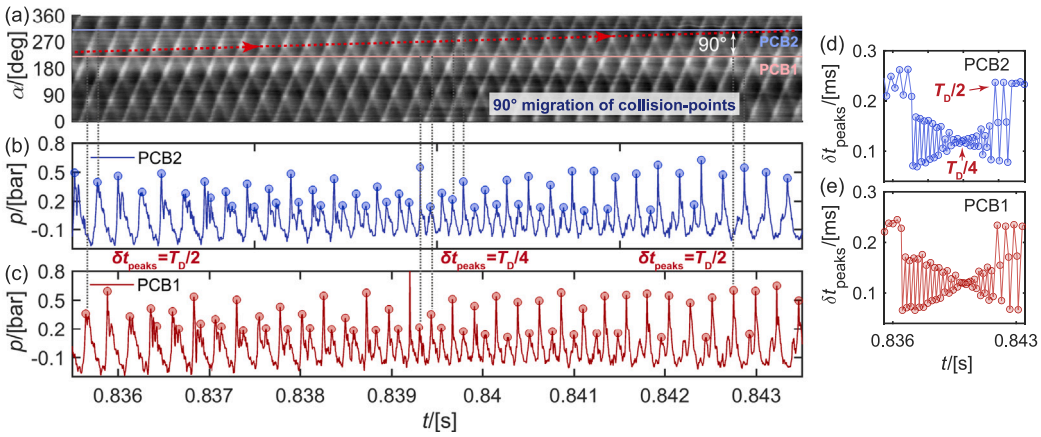


Fig. 7. Unidirectional 90° migration of collision points in the 4CR-CPM mode: (a) $x-t$ diagram and synchronous pressure signals from (b) PCB2 and (c) PCB1 in Case E2. (d)(e) Corresponding "X-shaped" variation patterns of peak intervals δt_{peaks} extracted from PCB2 and PCB1 signals.

To examine detonation propagation instabilities induced by air dilution, Case E2 is further analyzed based on the pressure signal and $x-t$ diagrams in Fig. 8. Peak-interval calculation and auto-correlation analysis [28,37] are combined to assess detonation propagation periodicity and stability. Within each moving window centered at t_i, the auto-correlation time lag τ_i is determined as the location of the first non-zero local maximum of the normalized auto-correlation coefficient R_{xx}, also corresponding to the time interval between two successive pressure peaks. The mode adjustment after dilution is divided into four stages: undiluted propagation, transition, detonation attenuation, and mode recovery.

(1) Stage I: undiluted propagation. Before dilution, the unidirectional migration of collision points (Fig. 8(f1)) produces "X-shaped" patterns in δt_{peaks} (Fig. 8(d)). Utilizing the dominant frequency $f_p = 4.2$ kHz extracted from the STFT spectrum (Figs. 8(b)(c)), the DW velocity in four-wave collision modes can be calculated via

$$V_D = 2\pi R_o f_D = 2\pi R_o f_p / N, \tag{3}$$

where f_D is the propagation frequency of an individual DW. When collision points periodically coincide with the sensor location, δt_{peaks} equals $T_D/2$, yielding $f_p = 2f_D$ and an equivalent wave count of $N = 2$ in Eq. (3). This gives $V_D = 1178$ m/s, or 60.9% of V_{CJ}. This velocity deficit, consistent with reported two- and four-wave collision modes [31,32,38], reflects non-ideal detonation propagation associated with repeated wave weakening during collisions and incomplete reactant refilling.

(2) Stage II: transition. Once air injection begins at $t = 1.47$ s, DWs are first weakened and then undergo mode adjustment. The CPM is markedly decelerated with reduced DW velocity difference. The collision-point migration period T_{CPM} increases from 5.4–7.8 ms before dilution to 15.7 ms and 32.2 ms after dilution. During $t = 1.52$–1.56 s, subharmonic components at $0.5f_p$ emerge (Fig. 8(b)), indicating transient mode adjustment. The concurrent drop in normalized auto-correlation coefficient R_{xx} confirms enhanced detonation instability (Fig. 8(e)). Notably, this instability manifests in δt_{peaks} as a periodic alternation above and below $T_D/2 = 0.245$ ms, highlighted by the blue circle in Fig. 8(d) and enlarged in Fig. 8(h1). The corresponding auto-correlation time lag τ in Fig. 8(h2) exhibits similar oscillatory behavior.

A complete δt_{peaks} oscillation period over 5 ms ($t = 1.53$–1.535 s) is shown in the x–t diagram (Fig. 8(g1)). The CW pair initially strengthens while the CCW pair weakens. A velocity difference then develops between the two co-propagating CWs. CW1 propagates faster than CW2 (Fig. 8(i)), producing non-uniform DW trajectories (①in Fig. 8(g1)). As the velocity difference gradually diminishes during $t = 1.533$–1.535 s (② in Fig. 8(g1)), the wave spacing becomes nearly uniform again (Fig. 8(j)), completing one oscillation period. The adjacent peak intervals in Fig. 8(g2) correspondingly evolve from $\delta t_1 \approx \delta t_2$ to $\delta t_1 > \delta t_2$ and recover, with δt_{peaks} returning to $T_D/2$. This introduces a doubled modulation period of $2T_D$ and therefore the $0.5f_p$ subharmonic in Fig. 8(b), which represents a frequency-domain signature of wave-spacing oscillations induced by dilution air.

(3) Stages III and IV: detonation attenuation and mode recovery. Under sustained dilution, both the peak pressure (Fig. 8(a)) and the extracted f_p (Fig. 8(c)) decrease markedly, indicating reduced detonation strength. The self-luminescence trajectories in Fig. 8(f2) become diffuse, suggesting slower chemical reactions and weakened shock-flame coupling. Reactant refilling then enables re-establishment of 4CR-CPM mode after $t = 1.73$ s with gradually decreasing T_{CPM} (Fig. 8(d)). The CPM direction shifts from counter-clockwise to clockwise (Fig. 8(f3)), and the wave-spacing oscillations persist (Fig. 8(d)).

5. Detonation instability induced by dilution jets

5.1. Timescale competition between jet recovery and detonation sweeping

Fig. 9 compares the auto-correlation time lag τ for Case E2 (η_{air} = 20%) with runtime dilution and Case E1 (η_{air} = 15%) with pre-ignition dilution. In both cases, τ oscillates around $T_D/2$ (0.245 ms for Case E2 and 0.25 ms for Case E1), reflecting alternating increases and decreases in the spacing between co-propagating DWs. Case E1 first maintains $\tau = T_D/2$ for a short interval after ignition, and then enters regular oscillation (Fig. 9(d)) as in Case E2 (Fig. 9(a)). This indicates that transverse air jets destabilize detonation propagation by non-uniformly weakening the waves and breaking the wave-strength balance, regardless of whether air is introduced before ignition or during engine operation.

Similar non-uniformly spaced waves with cyclic acceleration and deceleration, accompanied by sidebands around the dominant frequency, were reported by Johnson et al. [39]. They identified this repeatable instability as limit cycle oscillation (LCO) waves. Since a limit cycle denotes a periodic state whose amplitude and period are governed by system nonlinearity [40], the wave-spacing oscillation is hereafter termed LCO instability. This represents a self-sustained detonation wave adjustment under unsteady air perturbation. The LCO period T_{LCO} is obtained by differencing adjacent cycle-boundary nodes near $T_D/2$ in Figs. 9(a)(d), as magnified in Figs. 9(b)(e). The mean values and standard deviations are 4.4 ± 0.5 ms for Case E2 and 4.7 ± 0.3 ms for Case E1, respectively. The narrower deviation in Fig. 9(f) indicates more stable oscillation in Case E1. Notably, since $T_{LCO} \approx$

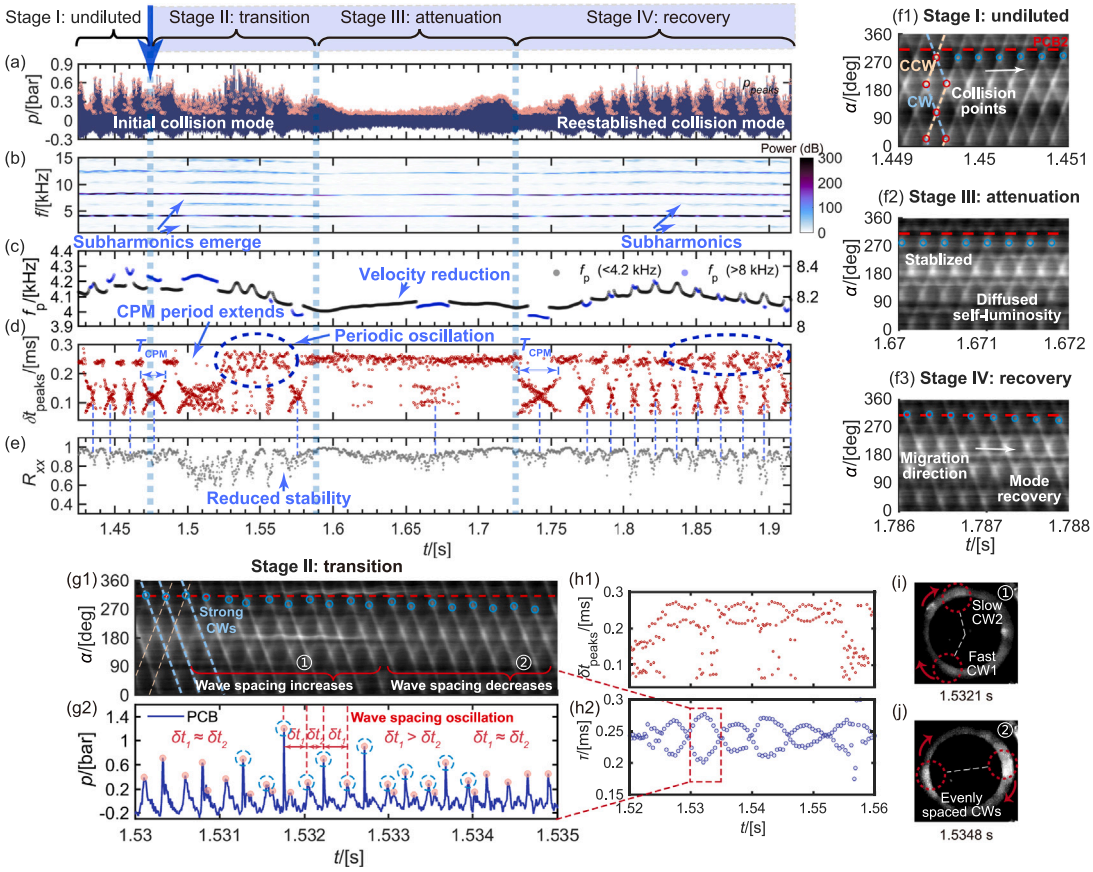


Fig. 8. Transient mode evolution in Case E2 under dilution. (a) PCB2 signal, (b) STFT spectrum, (c) dominant frequency f_p, (d) pressure-peak interval δt_{peaks}, and (e) normalized auto-correlation coefficient R_{xx}. (f1)-(f3) $x-t$ diagrams for Stages I, III, and IV. Stage II is detailed in the (g1) $x-t$ diagram, (g2) PCB2 signal, enlarged oscillations of (h1) δt_{peaks} and (h2) auto-correlation time lag τ, and HSC images showing (i) non-uniform and (j) nearly uniform wave spacing.

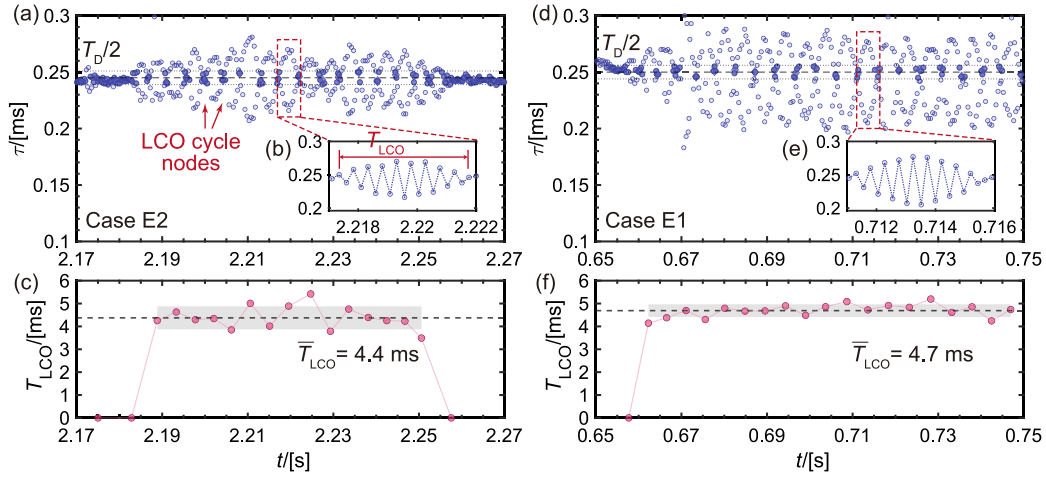


Fig. 9. (a)(d) Temporal evolution of the time lag τ for Case E2 with runtime dilution and Case E1 with pre-ignition dilution, magnified in (b)(e); (c)(f) extracted periods of limit cycle oscillation T_{LCO}.

7–11 T_D, the wave pair requires several propagation cycles to recover from a non-uniform to a nearly uniform distribution.

To quantify the nonlinear evolution characteristics of LCO instability, Poincaré maps of δt_{peaks} are constructed in Figs. 10(b)(e) to convert the pressure signal into phase-space trajectories between adjacent peak intervals $\delta t_{peaks,n}$ and $\delta t_{peaks,n+1}$. The diagonal $y = x$ represents equal successive peak intervals and serves as the reference for stationary collision points. In 4CR-CPM mode during the undiluted stage (Fig.

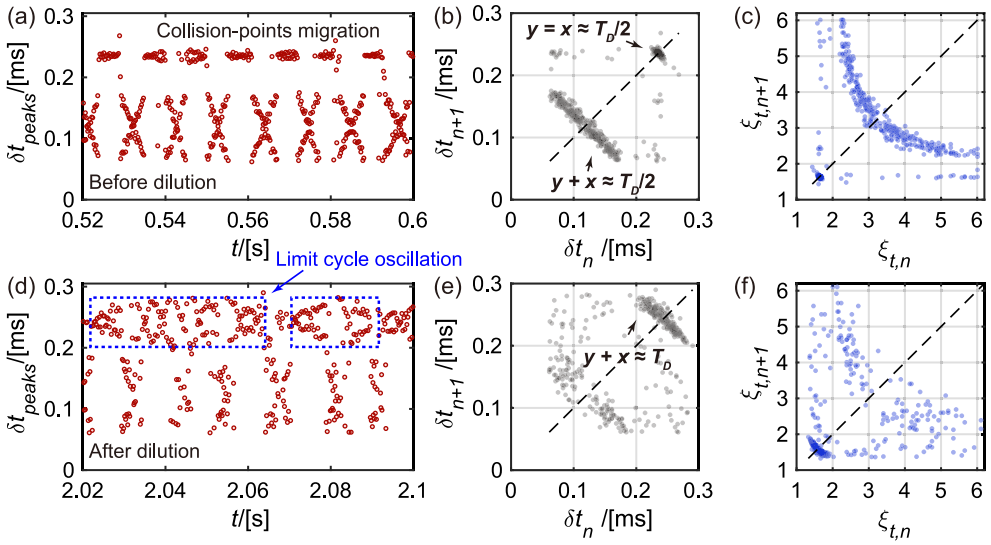


Fig. 10. Comparison of Case E2 (a)(b)(c) before and (d)(e)(f) after dilution. Temporal evolution of (a)(d) δt_{peaks}, (b)(e) Poincaré maps of δt_{peaks}, and (c)(f) Poincaré maps of the timescale ratio ξ_t.

10(a)) in Case E2, periodic collision point passage over the sensor produces partial clustering at $\delta t_{\text{peaks},n} = \delta t_{\text{peaks},n+1} = T_{\text{D}}/2 = 0.238$ ms (Fig. 10(b)). The remaining trajectories in Fig. 10(b) approximately satisfy the inverse variation relationship of adjacent peak intervals in Eq. (2).

In contrast, air dilution induces LCO instability and periodic oscillations of δt_{peaks} around $T_{\text{D}}/2$ in Fig. 10(d). Unlike Eq. (2), the corresponding map in Fig. 10(e) approximately follows

$$\delta t_{\text{peaks},n} + \delta t_{\text{peaks},n+1} \approx T_{\text{D}}. \tag{4}$$

The onset of LCO instability can be interpreted through the competition between jet recovery and successive DW sweeping. A timescale ratio is defined as

$$\xi_t = \frac{t_{\text{jet}}}{t_{\text{det}}}, \tag{5}$$

where t_{jet} is the characteristic re-establishment time of the transverse jet after transient blockage by DWs, and t_{det} is the interval between successive DW passages over the same dilution hole. Accordingly, ξ_t measures whether the air jet can re-establish a cold-air packet before the next wave passage. Physically, three regimes can be identified:

1. When $\xi_t \gg 1$, $t_{\text{jet}} \gg t_{\text{det}}$: the air jet recovers more slowly than detonation sweeping and is blocked before fully developing, limiting its penetration and influence on DW propagation;
2. When $\xi_t \sim O(1)$, $t_{\text{jet}} \approx t_{\text{det}}$: comparable timescales interrupt jet development before its characteristic structure is established, triggering mode adjustment and LCO instability;
3. When $\xi_t \ll 1$, $t_{\text{jet}} \ll t_{\text{det}}$: the jet develops sufficiently between DW passages, enhancing penetration and mixing, thereby non-uniformly weakening DWs and promoting LCO instability.

Thus, $\xi_t \leq O(1)$ provides a characteristic criterion for the onset of LCO instability. Since the dominant shear-layer scale is governed by the hole diameter d_{hole}, t_{jet} can be estimated by the convective timescale associated with the characteristic jet velocity V_{jet}:

$$t_{\text{jet}} = \frac{d_{\text{hole}}}{V_{\text{jet}}}. \tag{6}$$

Owing to the highly unsteady RDC flow field, direct experimental measurement of the instantaneous jet velocity is difficult. V_{jet} is therefore estimated using the mean bulk velocity through the dilution holes

$$V_{\text{jet}} = \frac{\dot{m}_{\text{d}}}{\rho_{\text{jet}} \cdot A_{\text{d}}}, \tag{7}$$

where ρ_{jet} is the dilution jet density. The mass flow rate through the dilution holes is $\dot{m}_{\text{d}} = \dot{m}_{\text{air}} - \dot{m}_{\text{c}}$, with $\dot{m}_{\text{c}}$ denoting the film-cooling air mass flow rate. The flow distribution between dilution and film-cooling air can be approximated by the area ratio, $\dot{m}_{\text{d}}/\dot{m}_{\text{c}} \approx A_{\text{d}}/A_{\text{c}} \approx 2.3$, where A_{d} and A_{c} are the total areas of the dilution and film-cooling holes, respectively. Over the tested $\dot{m}_{\text{air}} = 95$–$250$ g/s, the jet density ρ_{jet} is taken as 1.172 kg/m^3 at 300 K and 1 atm. Accordingly, V_{jet} is calculated as 20–53 m/s, corresponding to Mach numbers below 0.15, where the constant jet-density assumption is considered applicable under the present low Mach number conditions. Within each case, t_{jet} is approximated as constant, yielding 0.50, 0.37, 0.24, and 0.19 ms for comparative timescale analysis in Cases E1–E4, respectively.

In contrast, t_{det} varies during persistent CPM in four-wave collision modes. Since each peak interval δt_{peaks} represents the time between successive DW passages over the same dilution hole, $t_{\text{det}} = \delta t_{\text{peaks}}$. Accordingly, Figs. 10(c)(f) present the Poincaré maps of the timescale ratio, $\xi_{t,n+1} = f(\xi_{t,n})$, derived from the corresponding maps of δt_{peaks} in Figs. 10(b)(e).

Before dilution, substituting $\xi_{t,n} = t_{\text{jet}}/\delta t_{\text{peaks},n}$ and $\xi_{t,n+1} = t_{\text{jet}}/\delta t_{\text{peaks},n+1}$ into Eq. (2) gives

$$\xi_{t,n+1} = \frac{\xi_{t,n}}{A_1 \xi_{t,n} - 1}, \tag{8}$$

where $A_1 = T_{\text{D}}/(2t_{\text{jet}})$ is a constant. Note that ξ_t increases as t_{det} decreases. For example, immediately after DW sweeping in 4CR-CPM mode, $t_{\text{det}} = 0.069$ ms gives $\xi_t \approx 5.5$ in Fig. 10(c), indicating strongly suppressed jet recovery. In the next DW propagation cycle, t_{det} increases to 0.168 ms and ξ_t decreases to about 2.3 in Fig. 10(c), allowing partial jet penetration. Thus, the phase-space distribution of ξ_t reflects the jet response state between successive DW sweeps. The asymptotes at $\xi_{t,n} = 1/A_1$ and $\xi_{t,n+1} = 1/A_1$ of the hyperbolic mapping in Eq. (8) correspond to the maximum detonation sweeping interval $t_{\text{det}} = T_{\text{D}}/2$. For Case E2, $t_{\text{jet}} = 0.37$ ms yields asymptotes $\xi_{t,n} = 1.51$ and $\xi_{t,n+1} = 1.51$, consistent with the scatter distribution in Fig. 10(c). The separate cluster near $(1/A_1, 1/A_1)$ corresponds to $\delta t_{\text{peaks},n} = \delta t_{\text{peaks},n+1} = T_{\text{D}}/2$ when the collision points align with the sensor.

After dilution, Eq. (4) yields a similar hyperbolic mapping with $A_2 = 2A_1 = T_{\text{D}}/t_{\text{jet}}$. The scatter distribution in Fig. 10(f) intersects the diagonal $y = x$ at $(2/A_2, 2/A_2) = (1/A_1, 1/A_1)$, corresponding to the points at $\delta t_{\text{peaks},n} = \delta t_{\text{peaks},n+1} = T_{\text{D}}/2$ in Fig. 10(e). Notably, the ξ_t points in Fig. 10(f) spread around the diagonal more strongly than the separate cluster near $(1/A_1, 1/A_1)$ before dilution in Fig. 10(c). This occurs because Eq. (4) physically describes δt_{peaks} oscillations around

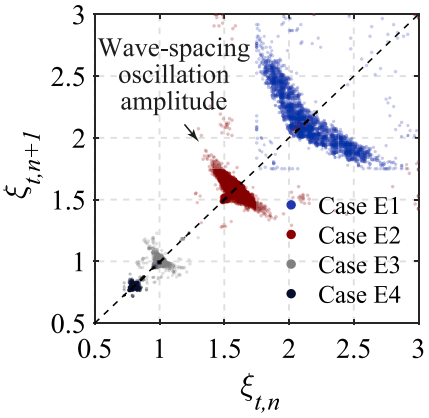


Fig. 11. Experimental Poincaré maps of the timescale ratio ξ_t for Cases E1–E4 under different dilution air flow rates.

$T_D/2$ during LCO instability. Larger departures from the diagonal therefore indicate stronger δt_{peaks} fluctuations and enhanced wave-spacing oscillations within each LCO period T_{LCO}.

Fig. 11 compares Poincaré maps of ξ_t for pre-ignition dilution Case E1 and runtime dilution Cases E2–E4, with increasing η_{air}. As $\dot{m}_{air}$ increases, the higher V_{jet} shortens t_{jet} and decreases ξ_t. This shifts the diagonal intersections $(1/A_1, 1/A_1)$ toward the origin, with coordinates of $(2,2)$, $(1.51,1.51)$, $(0.98,0.98)$, and $(0.77,0.77)$ for Cases E1–E4, respectively. Cases E1 and E2 with lower $\dot{m}_{air}$ remain $\xi_t > 2$ and $\xi_t > 1.51$, respectively, indicating limited impact of transverse jets on DW propagation. Stronger dilution in Cases E3 and E4 drives ξ_t toward $O(1)$, entering the jet-detonation timescale competition regime and promoting enhanced jet penetration.

Meanwhile, the reduced deviation from the diagonal in Cases E1–E4 indicates reduced wave-spacing oscillation amplitudes, as stronger dilution weakens DWs and suppresses wave strength differences. The experiments indicate that the influence of dilution jets on detonation instability is governed by the jet recovery timescale relative to DW sweeping, rather than by the air flow rate alone. Accordingly, ξ_t serves as a characteristic scaling parameter to identify when transverse jets become dynamically coupled with DW propagation and thereby induce global mode adjustment and detonation instability in RDTEs.

5.2. Feedback mechanism of wave-spacing oscillation

This section further elucidates the self-sustained mechanism of LCO instability. Unlike quasi-steady jet mixing in conventional combustors, downstream dilution in a RDC occurs under repeated sweeping of high-speed oblique shocks. The unsteady pressure drop across the orifices drives pulsating air injection, intermittent jet penetration, and discrete cold-air pockets, thereby imposing non-uniform disturbances on DW propagation. The resulting wave-strength imbalance drives spacing oscillations of co-propagating DWs and the onset of LCO instability.

The wave-spacing oscillation is sustained by a nonlinear feedback loop. As shown in Figs. 8(i)(j), a four-wave collision mode comprises two counter-rotating wave pairs, and LCO instability involves pronounced strength imbalance between the two DWs within one co-propagating pair. The feedback mechanism is therefore examined via the clockwise pair CW1/CW2 in Fig. 12, where blue arrows indicate air-jet penetration. Initially, CW1 and CW2 have comparable strength. If non-uniform dilution weakens CW2 during the ith cycle, CW2 slows relative to CW1 ($V_{D,2} < V_{D,1}$) and lags behind (Fig. 12(a)). The subsequent evolution is governed by two effects: wave attenuation caused by air jet penetration and reactant accumulation regulated by wave spacing. Over gradual spacing adjustments spanning $k = T_{LCO}/T_D$ wave propagation cycles, these effects alternately dominate and drive one complete wave-spacing oscillation period through two stages:

Wave-spacing growth stage (Fig. 12(a)): as CW2 lags behind CW1, the enlarged spacing allows longer jet recovery time and deeper penetration ahead of CW2, further weakening it. In contrast, the shorter jet recovery time ahead of CW1 results in less wave attenuation. Thus, $V_{D,1}$ increases relative to $V_{D,2}$, further amplifying the spacing between CW1 and CW2;

Wave-spacing recovery stage (Fig. 12(b)): once the spacing reaches a maximal threshold, longer injection refilling time ahead of the slower CW2 promotes reactant accumulation, strengthens CW2 and raises $V_{D,2}$, while $V_{D,1}$ correspondingly decreases. By the $(i+k)$th cycle, two DWs recover comparable velocities ($V_{D,2} \approx V_{D,1}$), restoring nearly uniform spacing.

The recovered balance remains susceptible to non-uniform dilution, so local wave weakening can trigger the next spacing-growth stage. The nonlinear feedback sustains a self-organized oscillation in which DW strength and spacing adjust alternately under the competition between energy gain associated with fresh-reactant accumulation and energy loss caused by dilution-air disturbance. Thus, LCO instability emerges when these two effects become comparable, allowing DWs to maintain a dynamic, periodically adjusted balance. The dilution jet therefore acts as an intrinsically unsteady aerodynamic boundary strongly coupled to detonation dynamics.

The LCO instability is particularly evident in the present four-wave collision modes, whose sensitivity to wave-strength asymmetry induced by dilution jets makes them effective for exposing the underlying mechanism. Nevertheless, the feedback mechanism reflects a more general perspective on RDTE mode stability under unsteady aerodynamic disturbances. It suggests the existence of an intermediate dynamical regime between stable propagation and complete instability, sustained by periodic adjustment of wave strength and spacing.

6. Conclusion

This study investigated the detonation instability mechanisms induced by downstream transverse dilution jets in a methane-fueled open-loop rotating detonation turbine engine (RDTE). Experiments were conducted to clarify the effects of dilution jets on detonation attenuation, transient mode evolution, and unsteady jet-wave coupling. Key findings include:

Runtime air injection restricts the effective exhaust area and increases the combustor pressure, reducing the reactant injection pressure drop and the accumulation height ahead of detonation waves (DWs). As a result, stronger dilution causes transient detonation attenuation or even temporary decoupling. The subsequent pressure decrease partially restores reactant refilling, enabling shock-flame coupling and detonation mode recovery. Runtime dilution also causes transient turbine rotor acceleration. Peak rotor speed increases with air mass flow. During sustained RDTE operation beyond 2 min, the rotor approaches quasi-steady operation and reaches a maximum speed of 8000 rpm.

Upon dilution-air injection, the initial four-wave collision mode with collision-point migration undergoes a sequence of detonation mode evolution. Air injection first weakens the DWs and slows collision-point migration. Then, unlike quasi-steady mixing in deflagration combustors, the non-uniform dilution air disturbance breaks the wave-strength balance in the four-wave collision mode and produces periodic spacing oscillations between co-propagating waves, whether dilution is introduced before ignition or during operation. Each wave-spacing oscillation period spans 7–11 DW cycles via repeated adjustment from non-uniform to nearly uniform spacing, identified as limit cycle oscillation (LCO) instability.

The onset of LCO instability is governed by the competition between jet recovery and successive DW sweeping, quantified by the timescale ratio ξ_t. With increasing air flow rate, ξ_t decreases. When ξ_t approaches or falls below $O(1)$, jets penetrate more deeply between DW passages, strengthening jet-wave coupling and promoting detonation mode adjustment. Meanwhile, stronger dilution weakens the DWs and

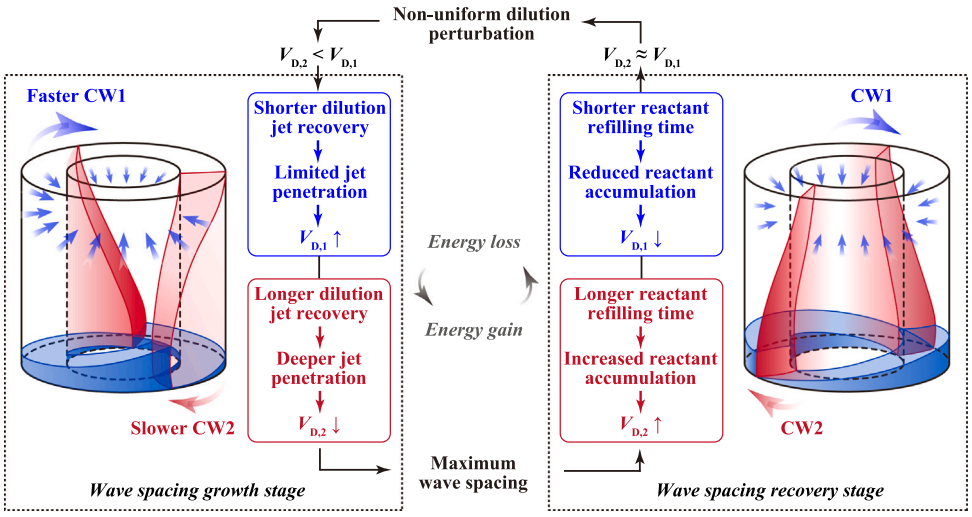


Fig. 12. Mechanism of wave-spacing oscillation induced by dilution air jets, illustrated using the co-propagating CW1 and CW2: (a) wave spacing growth stage, where enhanced air jet penetration weakens CW2; (b) wave spacing recovery stage, where increased reactant accumulation ahead of CW2 restores its strength.

suppresses wave-strength differences, thereby reducing wave-spacing oscillation amplitudes.

The LCO instability is sustained by a nonlinear feedback loop between cold-air penetration and reactant accumulation. Enlarged wave spacing allows deeper jet penetration and further weakens the slower DW, whereas longer reactant refilling later restores its strength, thereby recovering nearly uniform spacing. These findings reveal an intermediate dynamical regime between stable propagation and complete instability, sustained by periodic adjustment of wave strength and spacing, and provide a new perspective on mode stability limits in RDTEs under air dilution disturbances.

CRediT authorship contribution statement

Yuechen Hou: Writing – original draft, Visualization, Methodology, Investigation, Formal analysis. **Qi Sun:** Investigation. **Yingnan Wang:** Investigation. **Yiting Dang:** Investigation. **Zhuang Ma:** Investigation. **Zheng Chen:** Writing – review & editing. **Jianping Wang:** Writing – review & editing, Supervision, Funding acquisition, Conceptualization.

Declaration of competing interest

The authors declare that they have no known competing financial interests or personal relationships that could have appeared to influence the work reported in this paper.

Acknowledgments

This research was supported by the National Natural Science Foundation of China (Grant Nos. U25B20166 and 52506121).

References

[1] V. Anand, A. St. George, J. Jodele, E. Knight, E. Gutmark, Black-box modeling of rotating detonation combustors and their injector plena coupling, AIAA J. 58 (2020) 5095–5106.
[2] J. Sousa, G. Paniagua, E. Collado Morata, Thermodynamic analysis of a gas turbine engine with a rotating detonation combustor, Appl. Energy 195 (2017) 247–256.
[3] J.Z. Ma, M.-Y. Luan, Z.-J. Xia, J.-P. Wang, S.-J. Zhang, S.-B. Yao, B. Wang, Recent progress, development trends, and consideration of continuous detonation engines, AIAA J. 58 (2020) 4976–5035.
[4] R. Zhou, J.-P. Wang, Numerical investigation of flow particle paths and thermodynamic performance of continuously rotating detonation engines, Combust. Flame 159 (2012) 3632–3645.
[5] L. Su, F. Wen, S. Wang, Z. Wang, Analysis of energy saving and thrust characteristics of rotating detonation turbine engine, Aerosp. Sci. Technol. 124 (2022) 107555.
[6] F.A. Bykovskii, S.A. Zhdan, E.F. Vedernikov, Continuous spin detonation of a hydrogen-air mixture with addition of air into the products and the mixing region, Combust. Explos. Shock. Waves 46 (2010) 52–59.
[7] P. Wolański, Application of the continuous rotating detonation to gas turbine, Appl. Mech. Mater. 782 (2015) 3–12.
[8] P. Wolański, W. Balicki, W. Perkowski, A. Bilar, Experimental research of liquid-fueled continuously rotating detonation chamber, Shock Waves 31 (2021) 807–812.
[9] A. Naples, J. Hoke, R.T. Battelle, M. Wagner, F.R. Schauer, RDE implementation into an open-loop T63 gas turbine engine, in: 55th AIAA Aerospace Sciences Meeting, American Institute of Aeronautics and Astronautics, 2017, paper AIAA 2017-1747.
[10] S. Zhou, H. Ma, Y. Ma, C. Zhou, D. Liu, S. Li, Experimental study on a rotating detonation combustor with an axial-flow turbine, Acta Astronaut. 151 (2018) 7–14.
[11] C. Zhang, Z. Pan, Z. Lin, Rotating detonation wave propagation in axial flow turbine and continuous expansion combustor coupled structures, Fuel 399 (2025) 135221.
[12] R. Wang, S. Zhou, Study on a combustor of rotating detonation turbine engine with a jet-cooling structure, Case Stud. Therm. Eng. 72 (2025) 106456.
[13] S.-J. Liu, S.-Y. Huang, H.-Y. Peng, X.-Q. Yuan, Characteristics of methane-air continuous rotating detonation wave in hollow chambers with different diameters, Acta Astronaut. 183 (2021) 1–10.
[14] A. Naples, J. Hoke, F. Schauer, Rotating detonation engine interaction with an annular ejector, in: 52nd Aerospace Sciences Meeting, American Institute of Aeronautics and Astronautics, 2014, paper AIAA 2014-0287.
[15] R.T. Fievisohn, R. Battelle, M. Karimi, C. Klingshirn, Operation of a fully integrated rotating detonation combustor in a T63 gas turbine engine, in: ASME Turbo Expo 2024: Turbomachinery Technical Conference and Exposition, vol. Volume 5: Cycle Innovations, American Society of Mechanical Engineers, 2024, paper GT2024-122373.
[16] R. Huff, S. Boller, M. Polanka, F. Schauer, M. Fotia, J. Hoke, Radial rotating detonation engine driven bleed air turbine, J. Propul. Power 37 (2021) 252–260.
[17] J. Higashi, C. Ishiyama, S. Nakagami, K. Matsuoka, J. Kasahara, A. Matsuo, I. Funaki, H. Moriai, Experimental study of the disk-shaped rotating detonation turbine engine, in: 55th AIAA Aerospace Sciences Meeting, American Institute of Aeronautics and Astronautics, 2017, paper AIAA 2017-1286.
[18] C.A. Nordeen, V. Ahuja, S.B. Coogan, RDE diluent mixing & shock negation, in: AIAA Scitech 2021 Forum, American Institute of Aeronautics and Astronautics, 2021, paper AIAA 2021-0902.
[19] S.M. Frolov, A.V. Dubrovskii, V.S. Ivanov, Three-dimensional numerical simulation of the operation of the rotating-detonation chamber, Russ. J. Phys. Chem. B 6 (2012) 276–288.
[20] X.-J. He, X.-P. Gong, J.-P. Wang, J.Z. Ma, Investigation of the total pressure gain in rotating detonation combustors with dilution holes, Phys. Fluids 36 (2024) 045103.
[21] J. Yu, S. Yao, Y. Lei, W. Zhang, Rotating detonation combustor with regional full-coverage film cooling and variable-shaped hole arrangements, Phys. Fluids 37 (2025) 036112.

[22] D. Shen, M. Cheng, G. Rong, Z. Sheng, Y. Zhang, J. Wang, Effects of film cooling injection inclination angle on cooling performance in rotating detonation combustors, Phys. Fluids 36 (2024) 026118.
[23] J.D. Holdeman, Mixing of multiple jets with a confined subsonic crossflow, Prog. Energy Combust. Sci. 19 (1993) 31–70.
[24] K. Mahesh, The interaction of jets with crossflow, Annu. Rev. Fluid Mech. 45 (2013) 379–407.
[25] A.R. Karagozian, Transverse jets and their control, Prog. Energy Combust. Sci. 36 (2010) 531–553.
[26] J. Tobias, D. Depperschmidt, C. Welch, R. Miller, M. Uddi, A.K. Agrawal, R. Jr. Daniel, OH* chemiluminescence imaging of the combustion products from a methane-fueled rotating detonation engine, J. Eng. Gas Turbines Power 141 (2018) 021021.
[27] P. Liu, Y. Wang, X. Zhang, Y. Li, J.Z. Ma, J.-P. Wang, Experimental study on upstream pressure characteristics of rotating detonation engine with methane and oxygen-enriched air, Aerosp. Sci. Technol. 153 (2024) 109431.
[28] Y. Hou, P. Liu, Y. Li, Y. Dang, J.Z. Ma, J. Wang, Evolution dynamics and instability mechanisms of four-wave collisions in rotating detonation engines, Combust. Flame 282 (2025) 114466.
[29] F. Wang, C. Weng, H. Zhang, Semi-confined layered kerosene/air two-phase detonations bounded by nitrogen gas, Combust. Flame 258 (2023) 113104.
[30] R. Knystautas, Measurement of cell size in hydrocarbon-air mixtures and predictions of critical tube diameter, critical initiation energy and detonability limits, Prog. Astronaut. Aeronaut. 94 (1984) 23–37.
[31] E. Bach, P. Stathopoulos, C.O. Paschereit, M.D. Bohon, Performance analysis of a rotating detonation combustor based on stagnation pressure measurements, Combust. Flame 217 (2020) 21–36.
[32] X. Huang, C.J. Teo, B.C. Khoo, Wave mode dynamics in an ethylene-air rotating detonation combustor, AIAA J. 59 (2021) 1808–1823.
[33] D. Shen, J.Z. Ma, Z. Sheng, G. Rong, K. Wu, Y. Zhang, J. Wang, Spinning pulsed detonation in rotating detonation engine, Aerosp. Sci. Technol. 126 (2022) 107661.
[34] V. Anand, A. St. George, R. Driscoll, E. Gutmark, Longitudinal pulsed detonation instability in a rotating detonation combustor, Exp. Therm. Fluid Sci. 77 (2016) 212–225.
[35] C. Morley, Gaseq - a chemical equilibrium program for windows, 2005, version 0.79. http://www.gaseq.co.uk/.
[36] Y. Hou, Z. Sheng, D. Shen, Y. Zhang, G. Rong, J.Z. Ma, J. Wang, Mode evolution dynamics and the role of sustained pre-detonator ignition in a rotating detonation engine, Int. J. Hydrog. Energy 201 (2026) 152838.
[37] A.C.S. George, V. Anand, R.B. Driscoll, E.J. Gutmark, A correlation-based method to quantify the operating state in a rotating detonation combustor, in: 54th AIAA Aerospace Sciences Meeting, American Institute of Aeronautics and Astronautics, 2016, paper AIAA 2016-1402.
[38] R. Bluemner, M.D. Bohon, C.O. Paschereit, E.J. Gutmark, Effect of inlet and outlet boundary conditions on rotating detonation combustion, Combust. Flame 216 (2020) 300–315.
[39] K.B. Johnson May, J. Weber, D. Ferguson, A. Nix, T.G. Sidwell, Limit cycle oscillating detonation wave behavior analysis within a rotating detonation engine, J. Propul. Power 40 (2024) 701–716.
[40] S.H. Strogatz, Nonlinear Dynamics and Chaos: with Applications to Physics, Biology, Chemistry, and Engineering, third ed., Chapman and Hall/CRC, 2024.